JOURNAL OF GEOPHYSICAL RESEARCH, VOL. 111, B08303, doi:10.1029/2005JB004137, 2006

The M_w 7.8, 2001 Kunlunshan earthquake: Extreme rupture speed variability and effect of fault geometry

D. P. Robinson,[1] C. Brough,[1] and S. Das[1]

Received 2 November 2005; revised 19 January 2006; accepted 12 April 2006; published 11 August 2006.

[1] By analyzing body wave seismograms, we show that the rupture speed on the Main Kunlun Fault during the M_w 7.8 2001 Kunlunshan, Tibet, earthquake was highly variable and the rupture process consisted of three stages. In the first stage, the rupture accelerated from rest to an average speed of 3.3 km/s over a distance of 120 km. The rupture then propagated for another 150 km at an apparent rupture speed exceeding the *P* wave speed. In the final stage, the earthquake fault bifurcates, and the rupture front slowed down. The region of highest rupture velocity is found to coincide with the region of highest fault slip, has the longest slip duration, and is where off-fault ground cracking is observed in the field. Stress drops are found to be higher in regions of higher rupture speeds. The greatest concentration of aftershocks is located near the fault bifurcation zone and hence coincides with the region of highest fault slip, highest stress drop and highest rupture velocity. The fault width is no more than 10 km in most places and is about 20 km in the region of highest slip. This narrow fault width is attributed to the fact that crust below this depth is sufficiently warm not to permit brittle failure to occur. The remarkable similarity of this earthquake with the 1906 California earthquake, in spite of occurring in very different tectonic regimes, is discussed.

Citation: Robinson, D. P., C. Brough, and S. Das (2006), The M_w 7.8, 2001 Kunlunshan earthquake: Extreme rupture speed variability and effect of fault geometry, *J. Geophys. Res.*, *111*, B08303, doi:10.1029/2005JB004137.

1. Introduction

[2] It is now well known that the damage caused by an earthquake depends on the ground velocity and acceleration at the site, which in turn are controlled by the velocity and acceleration of the propagating fault [*Madariaga*, 1983]. Thus knowledge of the maximum possible speed at which earthquakes can propagate is essential for reliable seismic hazard assessment. In the 1960s, it was believed that earthquake ruptures could not propagate faster than the Rayleigh or shear wave speeds [*Broberg*, 1999; *Das*, 2003]. Theoretical rupture propagation studies in the 1970s [*Burridge*, 1973; *Hamano*, 1974; *Andrews*, 1976; *Das and Aki*, 1977; *Burridge et al.*, 1979; *Freund*, 1990] suggested that earthquakes could not only exceed the shear wave speed v_s but could actually propagate at the compressional wave speed v_p. For a long time, only one observation of supershear rupture speeds was found, namely for the 1979 Imperial Valley, California earthquake [*Archuleta*, 1984], but recent observations of supershear rupture speeds in laboratory experiments [*Rosakis et al.*, 1999; *Samudrala et al.*, 2002; *Xia et al.*, 2004] rekindled interest in searching for such speeds. Several such observations have now been reported [*Bouchon et al.*, 2001; *Bouchon and Vallée*, 2003; *Antolik et al.*, 2004; *Ozacar and Beck*, 2004; *Dunham and Archuleta*, 2004]. One of these was for the 14 November 2001 M_w 7.8 Kunlunshan, Tibet, earthquake during which an average supershear rupture speed was reported by *Bouchon and Vallée* [2003]. Since we know that rupture speed varies over the fault, we determine the details of the rupture process for this earthquake, in order to obtain the maximum rupture speed attained.

2. Tectonic Setting of the 2001 Kunlunshan Earthquake

[3] The 14 November 2001 M_w 7.8 Kunlunshan earthquake (Figure 1) ruptured an ~400 km portion of the Kunlun fault, a major strike-slip fault in central Tibet. Left-lateral motion along this fault is believed to accommodate some of the northward motion of the Indian plate under Tibet by lateral extrusion of the Tibetan crust. The rupture length in this earthquake is one of the longest for a strike-slip earthquake (for comparison, the 1906 San Francisco earthquake had a length of 432 km [*Yeats et al.*, 1997]) and is certainly the longest strike-slip faulting earthquake since the advent of modern seismometers. The Kunlunshan earthquake produced surface ruptures, reported from field observations, with displacements as high as 7–8 m [*Xu et al.*, 2002], this large value being supported by interferometric synthetic aperture radar (InSAR) measurements [*Lasserre et al.*, 2005]. Analysis of regional seismograms by *Bouchon and Vallée* [2003] suggested that the rupture propagated at an average speed of 3.9 km/s, which exceeded the local shear wave speed of 3.5 km/s. The supershear rupture speed was confirmed by analysis of *P* waves [*Antolik et al.*, 2004;

[1]Department of Earth Sciences, University of Oxford, Oxford, UK.

0148-0227/06/2005JB004137$09.00

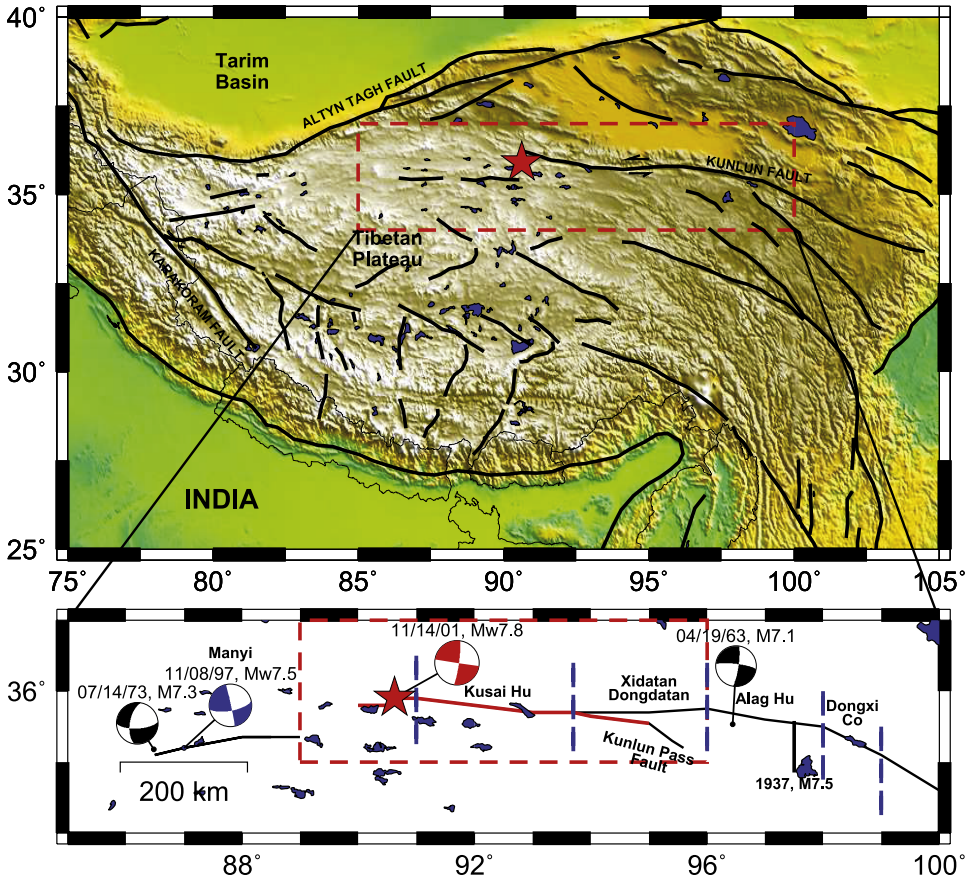

Figure 1. (top) Tectonic setting and topography in the region of the Kunlun Fault. The star indicates the epicenter of the 14 November 2001 Kunlunshan earthquake. (bottom) Segments [*Van der Woerd et al.*, 2002] of the Kunlun fault, shown by vertical blue dashed lines, together with the CMT solution obtained in this study (red). The Harvard CMT solution for the 8 November 1997 Manyi earthquake is shown in blue, and the focal mechanisms for two earlier earthquakes in the region with magnitudes $\geq$7 are shown in black [*Triep and Sykes*, 1997]. The faulting extent of the Kunlunshan earthquake is shown in red.

Ozacar and Beck, 2004], which gave an average speed of 3.4–3.6 km/s. In order to study the variability of the rupture speed over the fault, we use *SH* body waves to resolve the details of the rupture and fault slip histories.

3. Relocated Aftershocks

[4] We have relocated the aftershocks of this earthquake for the 6-month period following it, using the method of Joint Hypocenter Determination [*Dewey*, 1971, 1983] and *P* wave arrival times reported by the International Seismological Centre (ISC). The ISC reported 91 earthquakes during this period, with 41 having $m_b \geq 4.0$ and 8 with $m_b \geq 5.0$. Of these 91 earthquakes, we successfully relocated 80, with 73 of these having 90% confidence error ellipses $\leq$30 km. We consider these 73 earthquakes to be "reliably" relocated. The 80 aftershocks relocated by us for the 6-month period following the earthquake are shown in Figure 2. Only 5 earthquakes in this 6-month period have Harvard centroid moment tensor (CMT) solutions (Harvard CMT solutions for 1983–2002 can be accessed at http://www.seismology.harvard.edu/CMTsearch.html), the largest one on 18 November 2001 having a M_w of 5.6, which is remarkably small for such a large main shock. None of the five CMT solutions have the same mechanism as the main shock, suggesting that they either lie off the main fault or are indicative of small-scale fault plane complexity.

4. Centroid Moment Tensor Solution

[5] Since shallow vertical strike-slip faults have unstable centroid moment tensor (CMT) solutions [*Henry et al.*, 2002], we redo the CMT solution. The Harvard CMT solution was obtained using 44 stations and 123 channels, giving the solution with strike 94°, dip 61°, rake −12°, and a seismic moment M_0 of 5.9×10^{20} N m (equivalent to M_w of 7.8). Since the Harvard solution was obtained, many additional stations have reported data. We are thus able to recalculate the CMT solution using 89 stations and 243 channels and the same method as used by Harvard [*Dziewonski and Woodhouse*, 1983]. We find an optimal [*Henry et al.*, 2000] solution of strike 94°, dip 70°, rake −25°, and M_0 of 5.7×10^{20} N m, close to that found by Harvard. Since shallow crustal earthquakes are not expected to have a significant nondouble-couple components [*Henry et al.*, 2000, 2002; *Robinson et al.*, 2001] we next impose the pure double-couple constraint and find an optimum pure double-couple (OPDC) solution with strike 98°, dip 90°, rake −36° (Figure 2), and M_0 of 5.4×10^{20} N m with steeper dip but similar strike to the

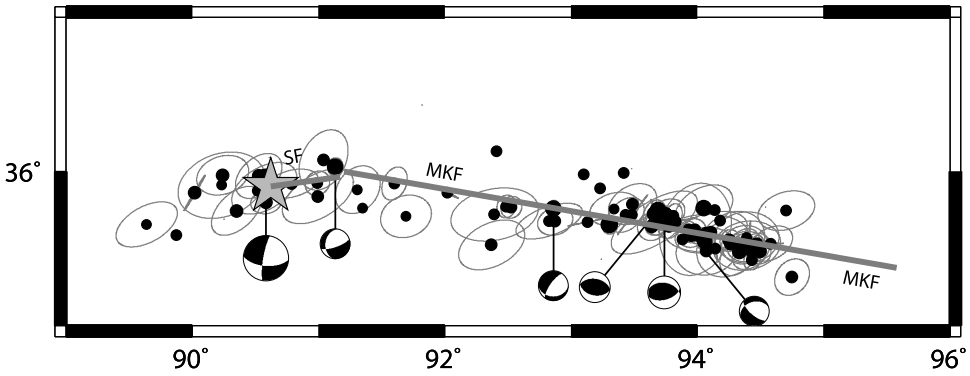

Figure 2. Relocated aftershocks for the 6-month period following the earthquake, shown as dots, with the symbol size scaling with magnitude. For aftershocks relocated "reliably," their location error ellipses are plotted in grey. The Main Kunlun Fault and the Secondary Fault are indicated by MKF and SF, respectively. Available Harvard CMT solutions for this time period are shown.

previous solutions. Since the dips of shallow strike-slip events are not well constrained [*Henry et al.*, 2000, 2002; *Robinson et al.*, 2001], we then carry out a grid search, for two values of strike (94° and 98°), over many values of dip and rake, with depth fixed, to examine the solution space. For each value of strike, we carried out 651 inversions. Figure 3 shows the misfit space for one value of strike (the other is similar and not shown). We see a broad region of possible solutions with misfit values only marginally higher than the OPDC solution given above. The general shape of this region is similar to such plots for other recent shallow strike-slip earthquakes, namely, the Antarctic Plate [*Henry et al.*, 2000] and Wharton Basin [*Robinson et al.*, 2001] earthquakes. Thus the mantle wave data are not able to provide an unambiguous source mechanism for this earthquake.

5. Analysis of Body Wave Seismograms

[6] To study the detailed faulting process, we use the method of seismogram inversion developed by *Das and Kostrov* [1990, 1994] and use pure *SH* waves at 19 stations, as well distributed in azimuth as was available, at epicentral distances from 35°–70°. Outside this distance range, unmodeled phases such as *ScS* or *SS* arrive very soon after the *S* wave making the usable part of the seismogram very short. At distances where no such phase arrives, we terminate the seismogram at 190 s. The source time is ~120 s, and 12 of the 19 stations have seismograms longer than 120 s, 8 of which are longer than 150 s. For similar reasons, the usable part of the pure *P* wave seismograms are very short, and too few stations were available to be used. To model Green's functions, we use the crustal model CRUST 5.1 [*Mooney et al.*, 1998] at the source and one modified from CRUST 5.1 for each station, based on known local geological conditions. The seismograms were filtered to contain periods between 2 and 120 s. However, due to attenuation of S waves in the mantle, the seismograms contain very little energy at periods less than 10 s. Thus, at first glance it may appear that we may not be able to image details of the rupture process. In order to understand better the resolution power of data of this type, we have carried out extensive numerical experiments with artificial teleseismic data in the 2–120 s period range, which we have then inverted using the same method as used in this paper for some earthquakes [*Henry et al.*, 2000; *Henry and Das*, 2002]. Such studies have shown that we are, in fact, able to image details smaller than might be expected. On the basis of this

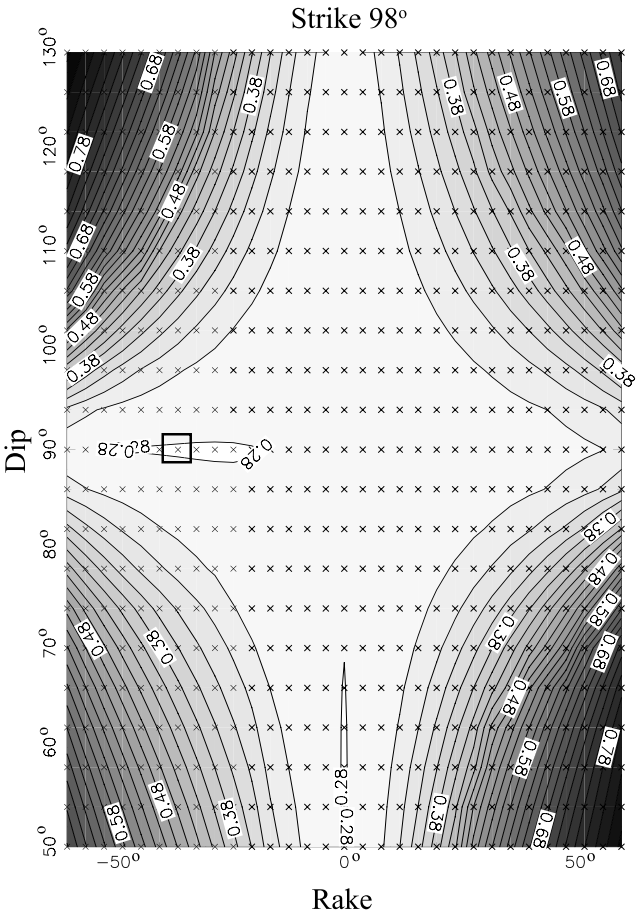

Figure 3. Contour plot of the variance ratio, minimized with respect to scalar moment, centroid longitude, latitude and time, plotted for double-couple moment tensors at depth 15 km and strike 98° and for a range of dips and rakes given. The square indicates the location of the OPDC solution found in this study.

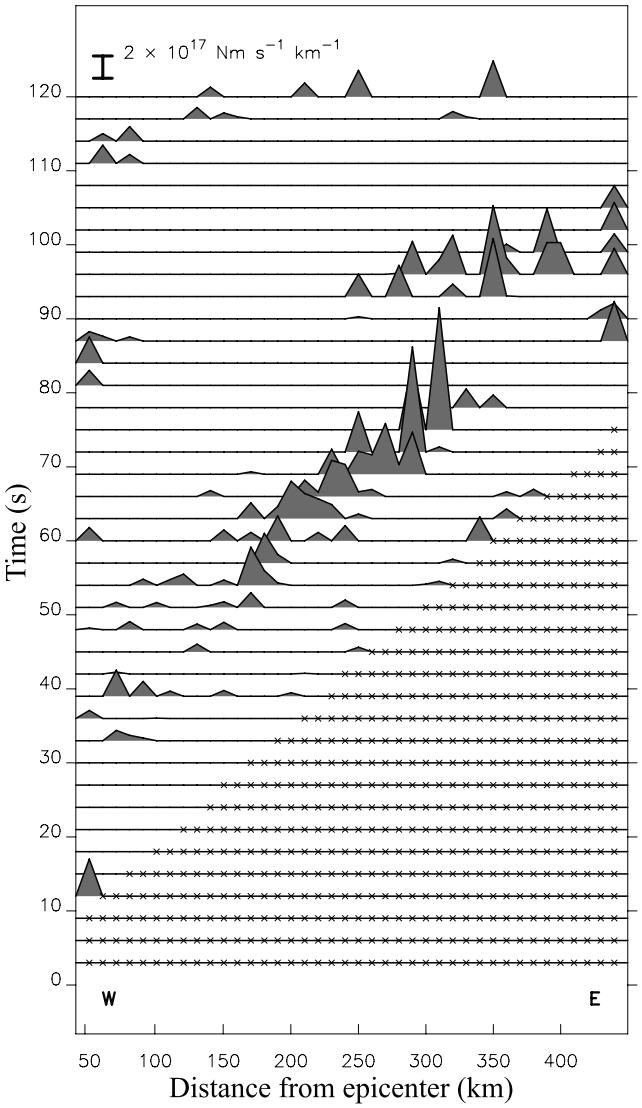

Figure 4. Rupture history for the MKF in our primary solution, which is used as a starting point to obtain our preferred solution, shown later. The spatial cell size used was 10 km, and the temporal cell size was 3 s. The moment rate per cell, along strike, summed along fault width, is shown at each time step, clearly highlighting the advancing rupture front. Crosses indicate cells on the fault that are prevented from slipping by causality (*P* wave causal front of 6 km/s was used in this case). The inversion solves the matrix equation with 2465 equations and 2226 unknowns. Comparison of fit of the data to the solution synthetics and the source time function are nearly identical to the solution shown in Figure 5 and are therefore omitted. The misfit value, ℓ_1, defined as the ratio of mean absolute error of fit to the mean absolute amplitude of the data is 0.445. Note that most studies report the square of a similar value in ℓ_2; for the sake of making comparisons of fit with other studies, the square of our value is 0.198.

experience, we have used a spatial cell size of 10 km for the discretization of the fault here. It is interesting to note that similar numerical experiments on artificial strong ground motion data also led to a similar conclusion [*Das and Suhadolc*, 1996; *Das et al.*, 1996; *Sarao et al.*, 1998], so that this behavior holds at very different length scales.

5.1. Optimal Source Mechanism for Use in Rupture Process Inversions

[7] Since the mantle wave data do not provide an unambiguous source mechanism, we must first obtain this. Attempts at inversions of the *SH* wave data using the source mechanisms obtained from our mantle wave study show that the initial parts of the seismogram are poorly fit. An earlier study [*Antolik et al.*, 2004] using *P* waves suggested that more than one fault was required to fit that data. We find that at least two faults are needed to fit the data. A third short fault placed in between these two faults, as was done by *Antolik et al.* [2004], has no perceptible effect on our data fit. We shall refer to these two faults as the Main Kunlun Fault (MKF) and the Secondary Fault (SF), as marked in Figure 2.

[8] In order to investigate the early portion of the rupture history, we carried out about 60 inversions, in which we vary the source mechanism, using a 80 km fault and the first 20 s of the *SH* data. This analysis reveals that the SF is best fit with strike 262°, dip 81° and rake −2°. This is very close to the *P* wave first motion solution [*Antolik et al.*, 2004]. We then use the entire *SH* wave seismogram picked at each station, fix the source mechanism of the SF and carry out about 80 further inversions to obtain the best fitting mechanism of the MKF as strike 100°, dip 90° and rake 7°, using a 400 km long fault for the MKF. Both the MKF and SF mechanisms fall in the broad minimum zone obtained from the mantle wave data (Figure 3).

5.2. Primary and Preferred Solutions

[9] Using these mechanisms, we obtain our primary solution, in which we use the positivity (no "back slip" on the fault) constraint; do not allow parts of the fault beyond a *P* wave from the hypocenter to rupture; and fix the total moment to our CMT solution moment. The rupture propagation with time is shown in Figure 4. Although the data are fitted well, the spatial moment distribution is seen to be very rough. Hence, following *Das and Kostrov* [1990, 1994], we find a "smeared out" solution in which the maximum moment rate anywhere on the fault at any time is minimized, keeping the fit to the data almost unchanged. This is our preferred solution, discussed from now on and shown in Figure 5. In our interpretation of the rupture process, our general conclusions are seen in both the primary and the preferred solutions, that is, we consider the persistent features of the solution, though it is the preferred solution that is discussed in detail. We use the terms 'slip' and 'moment' interchangeably in our discussions, as they are proportional to one another, the axes of figures always making it clear which quantity is being shown.

6. Rupture Process

[10] The rupture initiated at the westernmost end of the SF and propagated unilaterally eastward for ∼50 km. The rupture then continued along the MKF, with a change of strike from ∼82° to ∼100°, propagating eastward for another ∼400 km. Table 1 lists the source parameters

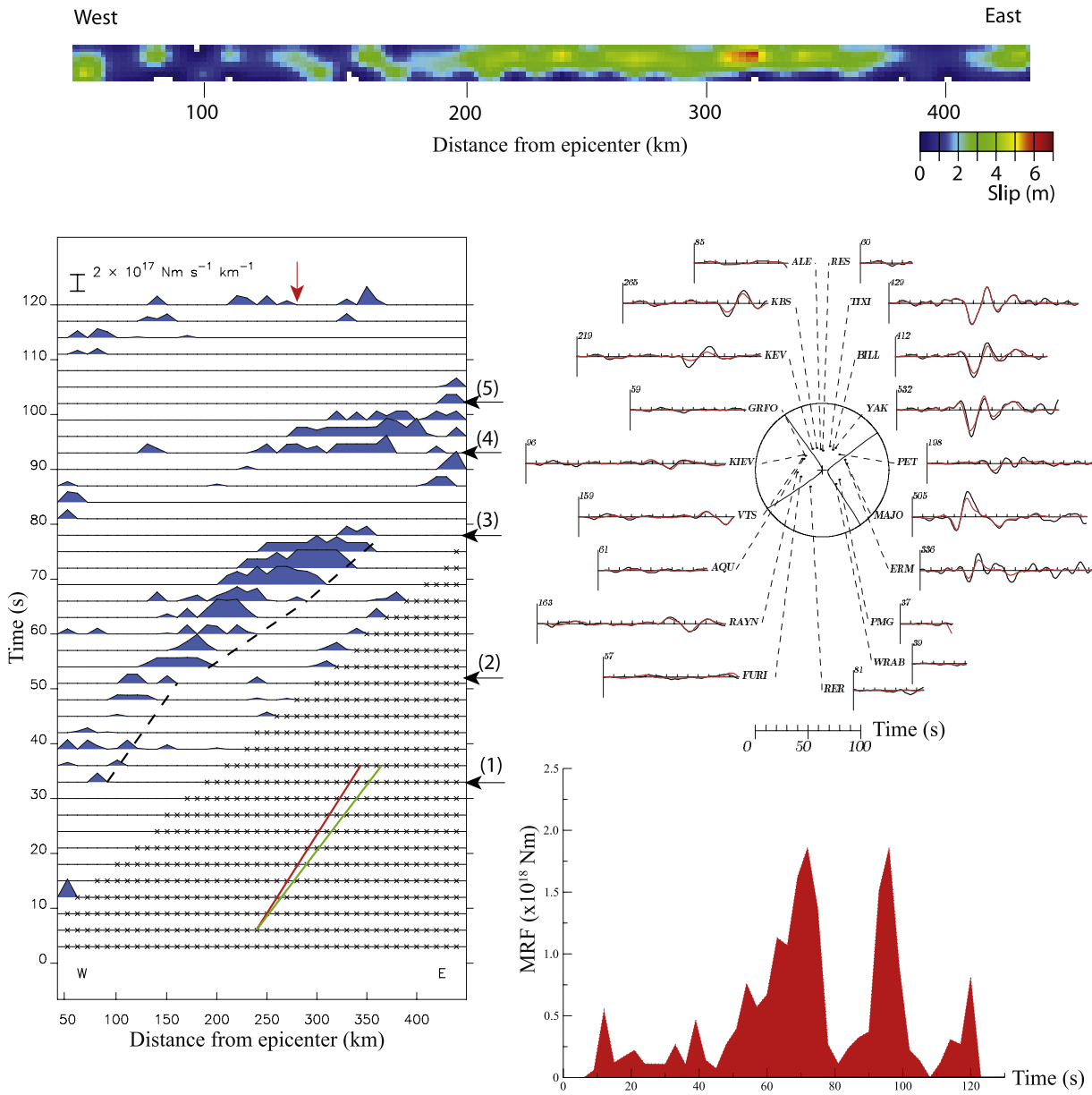

Figure 5. (top) Final slip on the MKF for our preferred solution. (bottom left) Same as Figure 4 but for our preferred solution. The dashed line indicates the approximate rupture front in the second stage of very rapid rupture. For comparison, two lines are drawn indicating the wave speeds of 4.1 (green) and 3.5 (red) km/s. Numerical noise seen adjacent to the *P* wave causal front is neglected. Arrows indicate the timing of (1) the start of main rupture on the MKF, (2) acceleration of rupture from 3.3 km/s to >6 km/s, (3) termination of rapid slip phase, and (4) beginning and (5) end of third phase of rupture. The arrow at the top indicates the fault bifurcation zone. (top right) Comparison of the *SH* wave data (black) with the solution synthetics (red), for our preferred solution (ℓ_1 misfit 0.467). The amplitude at each station is scaled to a constant distance of 60°, and the maximum amplitude in microns is shown at the beginning of each trace. Tick marks are placed at 10 s intervals along each trace. The *SH* nodal planes for the MKF for our preferred solution are shown on the stereographic projection of the focal sphere. (bottom right) Moment rate function for the earthquake from our preferred solution.

obtained for the two faults in our study. Figure 5 shows that the rupture process on the MKF consists of three distinct stages. The rupture propagated for the first 120 km on the MKF at an average speed of 3.3 km/s (94% of the local v_s). Note that since we have finite cells and time steps in our solution, all distances, times, rupture speeds and stress drops that we obtain are approximate. During the second stage, rupture continued eastward for another 150 km at a very high speed, the front being marked by a dashed line on Figure 5. The trend of the *P* wave causal zone (indicated by the crosses) helps to show that locally the rupture propagates in this stage at a speed exceeding the *P* wave speed.

Table 1. Source Parameters

Parameter	MKF	SF
Strike, deg	100	262
Dip, deg	90	81
Rake, deg	7	−2
Moment, $\times 10^{19}$ N m	55	4.3
Length, km	400	50
Width, km	20	20
Average rupture speed, km/s	4.1	1.3
Average slip, m	2.2	1.37
Average stress drop, MPa	2.4	1.5
Cell size, km	10 × 10	10 × 10
Time step, s	3	3
Modelled interval, s	0–120	0–45

It is important to note that this does not mean that rupture is acausal, since the front lies in the causal region. What it does mean is that when waves from the earlier parts of the rupture arrive, the rocks over this 150 km long region reach their breaking strength within a very short time interval, so that the apparent rupture speed (∼6.7 km/s) exceeds the *P* wave speed. Thus, in this stage, there is no ''classical'' rupture front. This possibility had been foreseen by *Kostrov* [1975] (and is discussed by *Kostrov and Das* [1988]), who considered an even more extreme case, that it is not impossible, though unlikely, that every point on a fault could reach its critical breaking stress simultaneously, making it appear to have infinite rupture velocity. As we see here, it is certainly possible for small sections of the fault to locally exceed the *P* wave speed.

[11] Figure 1 shows that near longitude 93.5°E, about 280 km east of the epicenter, the Kunlun fault bifurcates. Field evidence indicates that the rupture then propagated along the southern fork, the Kunlun Pass fault. The rupture history (Figure 5) shows that the second phase of apparently very rapid rupturing ends about 330–360 km east of the epicenter, with the earthquake then seeming to pause. The third stage of rupture commences after this pause. Though the rupture front so late into the rupture process is less well resolved, there is a definite further eastward progression of the front. The average speed for the entire rupture (SF and MKF) is 4.1 km/s. This agrees well with the surface wave study of *Bouchon and Vallée* [2003], who split the fault into four 100 km segments and found a preferred solution with a rupture velocity of 2.8 km/s in the first segment, 5 km/s in the second and third segments and were unable to resolve rupture velocity in the fourth segment well. However, it is slightly higher than previous body wave studies [*Lin et al.*, 2003; *Antolik et al.*, 2004; *Ozacar and Beck*, 2004] but is required to fit the *SH* wave data well. Table 2 gives the comparison of our results with previous body wave study results, showing the overall consistence of our solution with those. The final slip on the MKF is plotted in Figure 6 and shows that the region of highest rupture velocity coincides with the region of highest slip. The average slip on the MKF is found to be 2.18 m in our study. Using the relation

$$\Delta\sigma = \frac{2M_0}{\pi W^2 L},$$

where $\Delta\sigma$ is the stress drop, M_0 is the moment, and L and W are the length and width of the fault [*Scholz*, 1990], we find an average stress drop of 2.4 MPa, for a 400 km × 20 km fault. Estimated stress drop values in the three stages of rupture are approximately 1.6 MPa, 3.0 MPa and 2.5 MPa, respectively. Thus the fault slip and hence the stress drop increase as the rupture speed increases. We also see from Figure 5 that the region of very rapid rupture also has the longest slip duration.

6.1. Robustness Tests

[12] In order to examine the robustness of our results, in particular, the very high rupture speed obtained, we carry out additional tests. Initially, we constrain the average rupture speed not to exceed the local shear wave speed v_s (3.5 km/s). The corresponding solution is shown in Figure 7. The data are not fitted well and high moment piles up at the causal *S* wavefront, showing that rupture propagated faster than the shear wave for this earthquake. Next, we carry out several inversions constraining the average rupture speed to be less than 4.1 km/s (120% of v_s), 4.6 km/s (130% of v_s) and 5.5 km/s (160% of v_s, 90% of v_p), respectively. The rupture process when the average rupture speed is constrained not to exceed 4.6 km/s is shown in Figure 8. In all cases we find that the moment rate function is very robust and that large moment occurs in essentially the same region of the fault. The solution with average rupture speed constrained to be less than 5.5 km/s is almost identical to our preferred solution. For the other cases, moment is seen to be concentrated at the causal front, similar to that seen in Figure 7. We also conclude that the large slip at the easternmost end of the fault (Figure 6) is not very robust. Since we find that the high rupture speed occurs in the region of high moment, we carry out another level of optimization in which we attempt to minimize the moment in the region of the fastest rupture speed and still fit the data. We were unable to

Table 2. Comparison With Other Body Wave Studies

Study	Number of Stations	Data	L, km	W, km	u_{max},[a] m	X,[a] km	A[a] km	$\bar{\Delta\sigma}$,[a] MPa	$\Delta\sigma_a$,[a] MPa
This study	19	19 SH	400	20	6.5	94.3°E	50 × 20	2.4	8.0[b]
Lin et al. [2003]	17	17 P, 7 SH	400	30	6.8	93.1°E	60 × 30	1.2	7
Antolik et al. [2004]	37	35 P, 14 SH	400	15	10	93.2°E	60 × 15[c]	3.75	-
Ozacar and Beck [2004]	23	23 P	420	15	9	93.1°E	80 × 10[c]	3.1[d]	-

[a]The parameters are u_{max} is maximum slip on fault; X is location of main asperity; A is size of main asperity; $\bar{\Delta\sigma}$ is average stress drop on fault; $\Delta\sigma_a$ is stress drop on asperity.
[b]Calculated using the same method as *Lin et al.* [2003].
[c]Estimated from published diagrams.
[d]Calculated by us using published numbers.

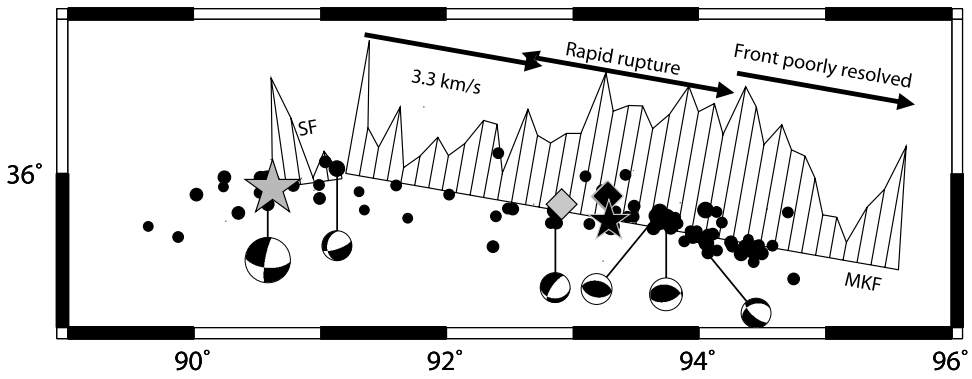

Figure 6. Schematic showing the final slip on the two faults, for our preferred solution, the maximum slip being 6.5 m. The average rupture speeds in the different stages of rupture are indicated. The Harvard CMT location (grey diamond), the location of the CMT solution obtained in this study (black diamond), and the centroid location of our broadband solution (black star) are shown.

remove the high moment in this region and still fit the data, showing that high moment in the region of the very rapidly rupturing portion of the fault is required by the data.

[13] Finally, we test if our not allowing rupture to occur ahead of the *P* wavefront from the hypocenter has affected the solution. For this we allow all points to rupture behind a causal front of 9 km/s. This is essentially equivalent to

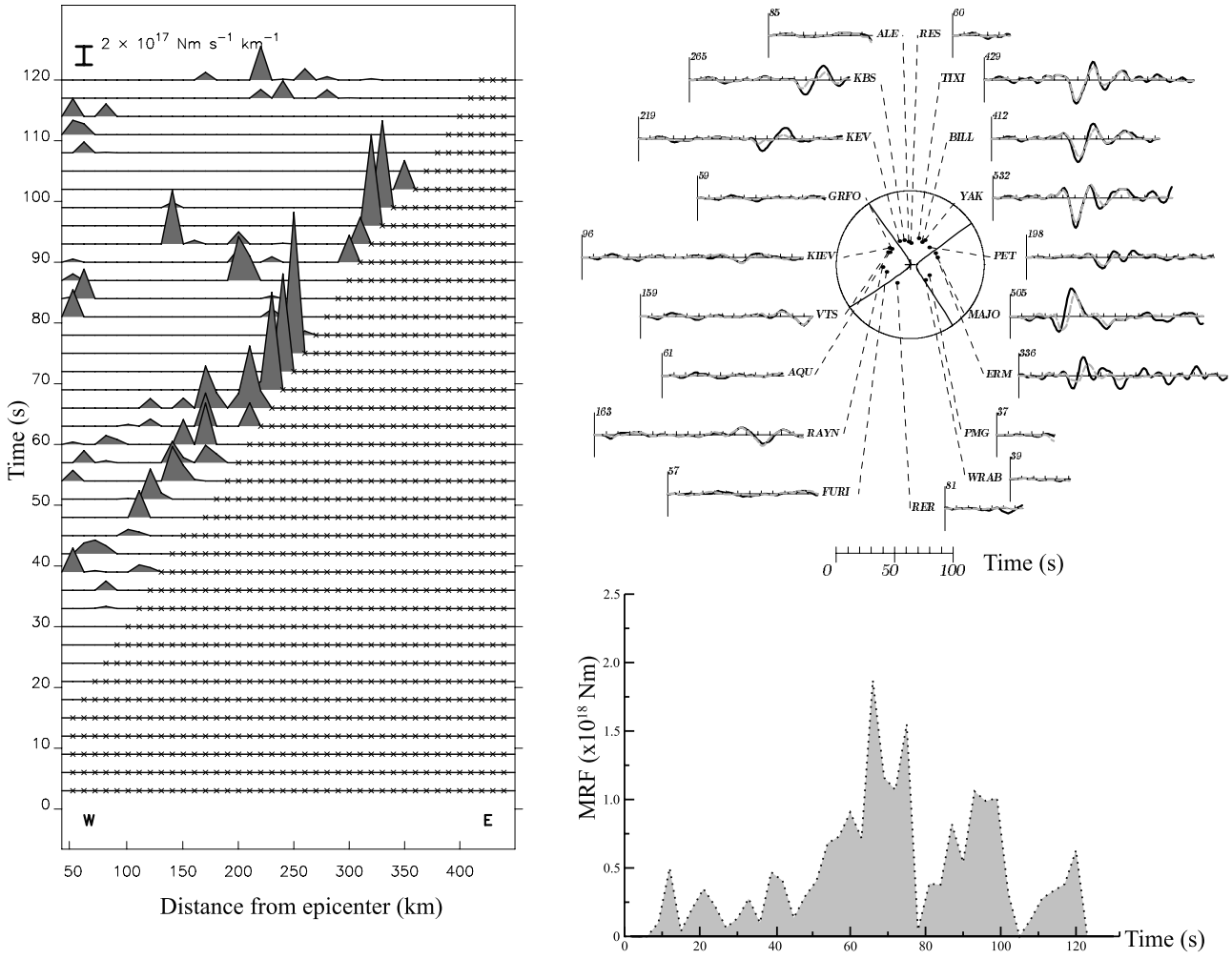

Figure 7. Similar to Figure 5 but for the case when we constrain the average rupture velocity not to exceed the local value of v_s of 3.5 km/s. The inversion is unable to satisfactorily fit the data (ℓ_1 misfit 0.567) and places the rupture front right up against the causality constraint, indicative of a faster rupture velocity being required.

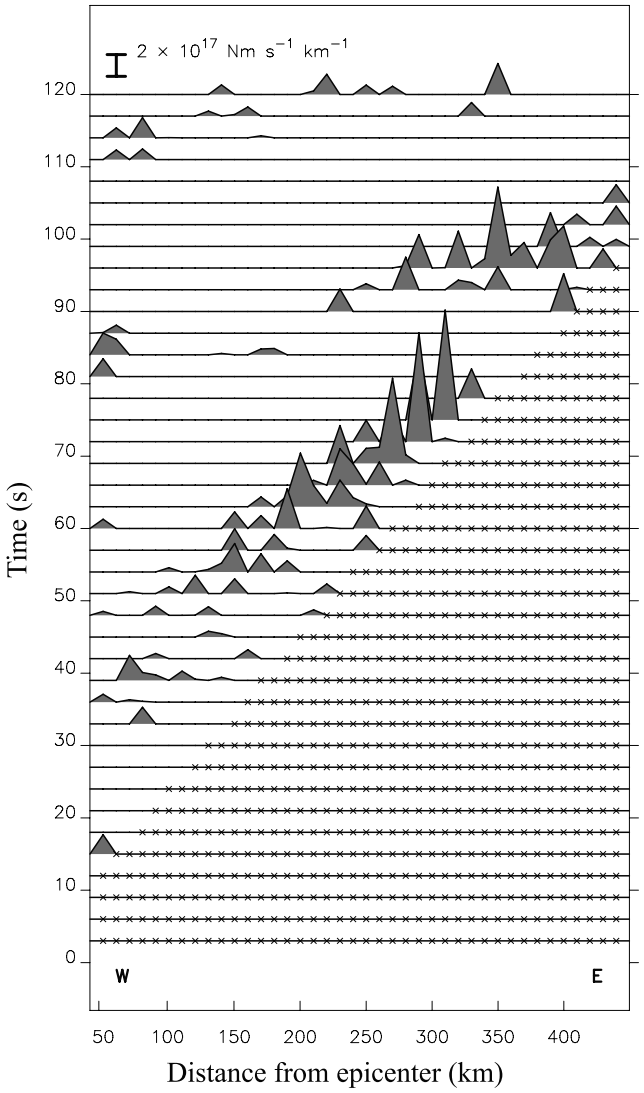

Figure 8. Similar to Figure 4 but for the case when the average rupture velocity is not permitted to exceed 4.6 km/s. The quality of fit to the data (ℓ_1 misfit 0.456) is not significantly worse than for our primary solution.

having no constraint at all on the rupture speed. The moment rate distribution in time is essentially identical to our preferred solution. In particular, no moment is seen ahead of the *P* wavefront, even though it is permitted. This gives us further confidence in our preferred rupture process.

[14] Theoretical models of supershear rupture propagation suggest that large stresses are generated in the off-fault regions and may cause fresh damage there (H. S. Bhat et al., Off-fault damage patterns due to supershear ruptures with application to the 2001 M_w 8.1 Kokoxili (Kunlun) earthquake, submitted to *Journal of Geophysical Research*, 2006, hereinafter referred to as Bhat et al., submitted manuscript, 2006). Field observations of anomalous ground cracking have been reported, concentrated in the region off-fault of the very fast rupture speed section of the fault for this earthquake (see photographs of Bhat et al. (submitted manuscript, 2006)).

6.2. Depth Extent of Faulting

[15] In order to determine the depth extent of coseismic faulting, a series of further inversions were carried out in which slip was constrained to occur at various depths. Our inversions showed that it is unlikely that there was any significant slip at a depth greater than 20 km, though in early inversions we permitted slip to occur to 40 km depth. Next, inversions where slip was constrained to occur in only the top 10 km were carried out. These inversions were able to fit the data almost, but not quite, as well as inversions where slip was permitted down to 20 km. However, when slip is constrained to the top 10 km, very large coseismic displacements of the order of 20 m are obtained, which does not agree with the surface observations [*Xu et al.*, 2002; *Lasserre et al.*, 2005]. Finally, a set of inversions were carried out where slip was confined only to depths between 10 and 20 km. These inversions were unable to satisfy the data. Therefore we conclude that slip extended to depths greater than 10 km, but less than 20 km.

[16] For our preferred solution, the final slip on the fault at each of the two cells levels, that averaged over the depth extent, and the measured surface displacements are shown in Figure 9. The slip in the region west of about 93°E is seen to be comparable in the upper and lower cells (Figures 5 and 9). However, when the fault is in the second stage of rupture, though the slip in the lower layer is markedly lower than the upper layer, it is still high compared to other parts of the fault (Figure 5). As the fault enters the third stage of rupture, beyond the bifurcation region, there is little slip in the lower layer, and most of the slip is confined to the top 10 km.

[17] The fact that no slip occurs below 20 km depth has important implications. First, theoretical studies show that on planes with constant properties, ruptures tend to be equidimensional [*Das*, 1981; *Das and Kostrov*, 1988; *Madariaga et al.*, 2000]. This earthquake is more than 400 km long yet no more than 20 km wide. So, there must be a very strong change in the properties near 20 km depth to prevent rupture from penetrating deeper. In well studied near-vertical strike-slip regimes such as the San Andreas fault, the seismogenic depth is also about 20 km, but there the reason is well understood, namely, that this is the crustal depth, below which material is too warm to permit brittle failure. The continental convergence zone of Tibet has a double thickness (~60 km) of crust. Therefore, at first glance, one could have expected a much larger fault width here and the fact that this does not occur may appear surprising. Crustal earthquake depths in this region are less than 20 km [*Chen and Molnar*, 1983], though there is also some evidence that earthquakes occur in the mantle to depths of 100 km [*Chen and Yang*, 2004]. However, there do not seem to be any earthquakes between about 20 and 70 km in this region. This agrees with recent studies of the temperature structure of the Tibetan crust by *Mechie et al.* [2004], who showed that the 700°C isotherm is likely to be at a depth of 18 km in this region, as the lower crust has been warmed as a result of burial and radioactive decay in the crust. This would prevent brittle failure below these depths and is thus similar to the seismogenic width of the San Andreas fault.

7. Discussion

[18] The 2001 Kunlunshan earthquake ruptured a clearly resolvable distance of nearly 150 km in a very short time

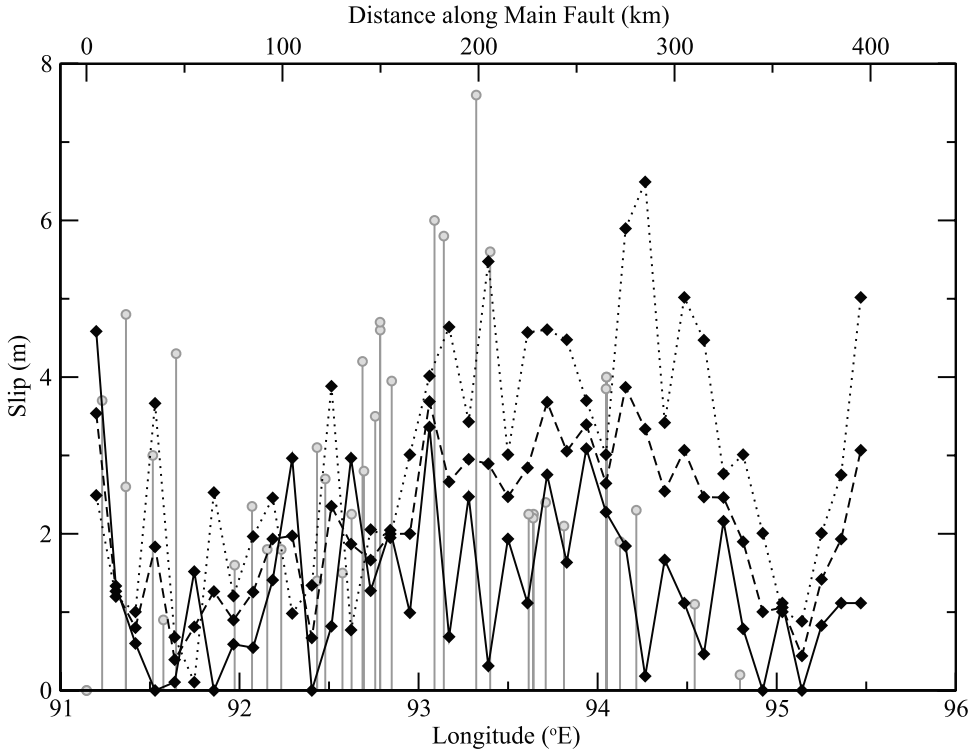

Figure 9. Along-strike displacement along the MKF, for our preferred solution, at the upper layer of cells (dotted line), the lower layer of cells (solid line), and averaged over the two layers (dashed line). The measured surface displacements [*Xu et al.*, 2002] are shown as discrete grey circles.

interval, leading to an apparent super-*P* wave rupture speed locally. This is the first observation of this phenomenon, foreseen by *Kostrov* [1975]. It has been suggested that the large length of the Kunlunshan earthquake was required for the fast rupture speed [*Xia et al.*, 2004]. Figure 1 shows that the MKF is also very straight for the first 270 km, the first and second stages of rupture propagation. Just after passing the bifurcation point, the rupture seems to pause before continuing on for the third stage along the southern fork, the Kunlun Pass Fault. Neither field nor InSAR observations show any coseismic movement on the northern fork, the Xidatan segment of the Kunlun fault [*Xu et al.*, 2002; *Lasserre et al.*, 2005]. This is a very good example of fault rupture being slowed by fault geometry. This fork is also the region with the highest concentration of aftershocks. The rupture terminates at a sharp change of strike (transition from red to black on the MKF in Figure 1), and we interpret this as a geometric barrier [*Aki*, 1979] which stops the rupture.

[19] Numerical experiments suggest that regions of faster rupture are also stronger [*Dunham et al.*, 2003], while the dimensionless parameter *S*, defined as the ratio of the relative fault strength to stress drop must be small [*Hamano*, 1974; *Andrews*, 1976; *Das and Aki*, 1977]. Our results showing that regions of fast rupture are also regions of higher stress drop shows how this is possible for the Kunlunshan earthquake.

[20] Even though the 2001 Kunlun earthquake occurred in a very different tectonic regime than the 1906 California earthquake, they are remarkably similar. Both are vertical strike-slip faults that have very similar lengths and widths, and unusually fast rupture speeds have been reported for both (by *Song et al.* [2005] for the 1906 earthquake).

[21] The most important and damaging earthquake of recent times was the 26 December 2004 great Sumatra earthquake [*Ammon et al.*, 2005]. It propagated for the first 600 km at an average speed of ~2.5 km/s, with the rupture velocities of later portions still being debated. This is much slower than the average rupture speed of the 2001 Kunlunshan earthquake. It should be noted that real faults rupture in a mixture of the two shear modes, the in-plane and the antiplane mode. The Kunlun earthquake fault was so long compared to its width that it was almost purely an in-plane fault. The 2004 Sumatra earthquake, with a down-dip width of about 200 km, was an antiplane fault along its strike but in-plane along the dip direction. This means that very long subduction zone thrust earthquakes, such as the Sumatra earthquake, could have a very long in-plane rupture front, which, in principle, could reach speeds as high as that for the Kunlun earthquake. However, no observation of supershear rupture speed has yet been reported for any subduction zone earthquake. Whether this is because this has never occurred, or, is due to the fact that seismic stations were not situated in optimal positions to detect this is not known. Obviously, detecting the along-dip rupture velocity is far more difficult than the along-strike speed.

[22] Our finding on how wide a range the rupture speeds of large earthquakes can span has important consequences for seismic hazard assessment, earthquake

engineering, and fundamental understanding of earthquake fracture mechanics.

[23] **Acknowledgment.** D.P.R. is supported by the U.K. NERC studentship NER/S/A/2003/11309 and a Schlumberger CASE award.

References

Aki, K. (1979), Characterization of barriers on an earthquake fault, *J. Geophys. Res.*, *84*, 6140–6148.

Ammon, C. J., et al. (2005), Rupture process of the 2004 Sumatra-Andaman earthquake, *Science*, *308*, 1133–1139.

Andrews, D. J. (1976), Rupture velocity of plane strain shear cracks, *J. Geophys. Res.*, *81*, 5679–5687.

Antolik, M., R. E. Abercrombie, and G. Ekström (2004), The 14 November 2001 Kokoxili (Kunlunshan), Tibet, earthquake: Rupture transfer through a large extensional step-over, *Bull. Seismol. Soc. Am.*, *94*, 1173–1194.

Archuleta, R. (1984), Faulting model for the 1979 Imperial Valley earthquake, *J. Geophys. Res.*, *89*, 4559–4585.

Bouchon, M., and M. Vallée (2003), Observation of long supershear rupture during the magnitude 8.1 Kunlunshan earthquake, *Science*, *301*, 824–826.

Bouchon, M., M.-P. Bouin, H. Karabulut, M. N. Toksöz, M. Dietrich, and A. J. Rosakis (2001), How fast is rupture during an earthquake? New insights from the 1999 Turkey earthquakes, *Geophys. Res. Lett.*, *28*, 2723–2726.

Broberg, K. B. (1999), *Cracks and Fracture*, 752 pp., Elsevier, New York.

Burridge, R. (1973), Admissible speeds for plane-strain self-similar shear crack with friction but lacking cohesion, *Geophys. J. R. Astron. Soc.*, *35*, 439–455.

Burridge, R., G. Conn, and L. B. Freund (1979), The stability of a rapid Mode II shear crack with finite cohesive traction, *J. Geophys. Res.*, *84*, 2210–2222.

Chen, W. P., and P. Molnar (1983), Focal depths of intracontinental and intraplate earthquakes and their implications for the thermal and mechanical properties of the lithosphere, *J. Geophys. Res.*, *88*, 4183–4214.

Chen, W. P., and Z. Yang (2004), Earthquakes beneath the Himalayas and Tibet: Evidence for strong lithospheric mantle, *Science*, *304*, 1949–1952.

Das, S. (1981), Three-dimensional spontaneous rupture propagation and implications for earthquake source mechanism, *Geophys. J. R. Astron. Soc.*, *67*, 375–393.

Das, S. (2003), Dynamic fracture mechanics in the study of the earthquake rupturing process: Theory and observation, *J. Mech. Phys. Solids*, *51*, 1939–1955.

Das, S., and K. Aki (1977), A numerical study of two-dimensional rupture propagation, *Geophys. J. R. Astron. Soc.*, *50*, 643–668.

Das, S., and B. V. Kostrov (1988), An investigation of the complexity of the earthquake source time function using dynamic faulting models, *J. Geophys. Res.*, *93*, 8035–8050.

Das, S., and B. V. Kostrov (1990), Inversion for slip rate history and distribution on fault with stabilizing constraints: The 1986 Andreanof Islands earthquake, *J. Geophys. Res.*, *95*, 6899–6913.

Das, S., and B. V. Kostrov (1994), Diversity of solutions of the problem of earthquake faulting inversion. Application to SH waves for the great 1989 Macquarie Ridge earthquake, *Phys. Earth Planet. Inter.*, *85*, 293–318.

Das, S., and P. Suhadolc (1996), On the inverse problem for earthquake rupture. The Haskell-type source model, *J. Geophys. Res.*, *101*, 5725–5738.

Das, S., P. Suhadolc, and B. V. Kostrov (1996), Realistic inversions to obtain gross properties of the earthquake faulting process, *Tectonophysics*, *261*, 165–177.

Dewey, J. W. (1971), Seismic studies with the method of joint hypocenter determination, Ph.D. thesis, Univ. of Calif., Berkeley.

Dewey, J. W. (1983), Relocation of instrumentally recorded pre-1974 earthquakes in the South Carolina region, in *Studies Related to the Charleston, South Carolina, Earthquake of 1886–Tectonics and Seismicity*, edited by G. S. Gohn, *U.S. Geol. Surv. Prof. Pap.*, *1313*, Q1–Q9.

Dunham, E. M., and R. J. Archuleta (2004), Evidence for a supershear transient during the 2002 Denali earthquake, *Bull. Seismol. Soc. Am.*, *94*, S256–S268.

Dunham, E., P. Favreau, and J. M. Carlson (2003), A supershear transition mechanism for cracks, *Science*, *299*, 1557–1559.

Dziewonski, A. M., and J. H. Woodhouse (1983), Studies of the seismic source using normal-mode theory, in *Earthquakes: Observation, Theory, and Interpretation*, edited by H. Kanamori and E. Boschi, *Proc. Int. Sch. Phys. Enrico Fermi*, *85*, 45–137.

Freund, L. B. (1990), *Dynamic Fracture Mechanics*, 563 pp., Cambridge Univ. Press, New York.

Hamano, Y. (1974), Dependence of rupture time history on the heterogeneous distribution of stress and strength on the fault (abstract), *Eos Trans. AGU*, *55*, 352.

Henry, C., and S. Das (2000), The M_w 8.2, 17 February 1996 Biak, Indonesia, earthquake: Rupture history, aftershocks and fault plane properties, *J. Geophys. Res.*, *107*(B11), 2312, doi:10.1029/2001JB000796.

Henry, C., S. Das, and J. H. Woodhouse (2000), The great March 25, 1998 Antarctic Plate earthquake: Moment tensor and rupture history, *J. Geophys. Res.*, *105*, 16,097–16,119.

Henry, C., J. H. Woodhouse, and S. Das (2002), Stability of earthquake moment tensor inversions: Effect of the double-couple constraint, *Tectonophysics*, *356*, 115–124.

Kostrov, B. V. (1975), *Mechanics of the Tectonic Earthquake Focus*, 176 pp., Nauka, Moscow.

Kostrov, B. V., and S. Das (1988), *Principles of Earthquake Source Mechanics*, 286 pp., Cambridge Univ. Press, New York.

Lasserre, C., G. Peltzer, F. Cramp, Y. Klinger, J. Van der Woerd, and P. Tapponnier (2005), Coseismic deformation of the 2001 M_w = 7.8 Kokoxili earthquake in Tibet, measured by synthetic aperture radar interferometry, *J. Geophys. Res.*, *110*, B12408, doi:10.1029/2004JB003500.

Lin, A., M. Kikuchi, and B. Fu (2003), Rupture segmentation and process of the 2001 M_w 7.8 central Kunlun, China, earthquake, *Bull. Seismol. Soc. Am.*, *93*, 2477–2492.

Madariaga, R. (1983), High frequency radiation from dynamic earthquake fault models, *Ann. Geophys.*, *1*, 17–23.

Madariaga, R., S. Peyrat, and K. B. Olsen (2000), Rupture dynamics in 3-D: A review, in *Problems in Geophysics for the New Millennium: A Collection of Papers in Honor of Adam M. Dziewonski*, edited by E. Boschi, G. Ekström, and A. Morelli, pp. 89–110, Compositori, Bologna, Italy.

Mechie, J., S. V. Sobolev, L. Ratschbacher, A. Y. Babeyko, G. Bock, A. G. Jones, K. D. Nelson, K. D. Solon, L. D. Brown, and W. Zhao (2004), Precise temperature estimation in the Tibetan crust from seismic detection of the α-β quartz transition, *Geology*, *32*, 601–604.

Mooney, W. D., G. Laske, and T. G. Masters (1998), CRUST 5.1: A global crustal model at $5^\circ \times 5^\circ$, *J. Geophys. Res.*, *103*, 727–747.

Ozacar, A. A., and S. L. Beck (2004), The 2002 Denali fault and the 2001 Kunlun fault earthquakes: Complex rupture processes of two large strike-slip earthquakes, *Bull. Seismol. Soc. Am.*, *94*, S278–S292.

Robinson, D. P., C. Henry, S. Das, and J. H. Woodhouse (2001), Simultaneous rupture along two conjugate planes of the Wharton Basin earthquake, *Science*, *292*, 1145–1148.

Rosakis, A. J., O. Samudrala, and D. Coker (1999), Cracks faster than the shear wave speed, *Science*, *284*, 1337–1340.

Samudrala, O., Y. Huang, and A. J. Rosakis (2002), Subsonic and intersonic shear rupture of weak planes with a velocity weakening cohesive zone, *J. Geophys. Res.*, *107*(B8), 2170, doi:10.1029/2001JB000460.

Sarao, A., S. Das, and P. Suhadolc (1998), Effect of non-uniform station coverage on the inversion for seismic moment release history and distribution for a Haskell-type rupture model, *J. Seismol.*, *2*, 1–25.

Scholz, C. (1990), *The Mechanics of Earthquakes and Faulting*, 438 pp., Cambridge Univ. Press, New York.

Song, S., G. C. Beroza, and P. Segall (2005), Evidence for supershear rupture during the 1906 San Francisco earthquake (abstract), *Eos Trans. AGU*, *86*(52), Fall Meet. Suppl., Abstract S12A-05.

Triep, E. G., and L. R. Sykes (1997), Frequency of occurrence of moderate to great earthquakes in intracontinental regions, *J. Geophys. Res.*, *102*, 9923–9948.

Van der Woerd, J., et al. (2002), The 14 November 2001 M_w = 7.8 Kokoxili earthquake in northern Tibet (Qinghai province, China), *Seismol. Res. Lett.*, *73*, 125–135.

Xia, K., A. J. Rosakis, and H. Kanamori (2004), Laboratory earthquakes: The sub-Rayleigh-to-super-shear transition, *Science*, *303*, 1859–1861.

Xu, X., et al. (2002), Surface rupture of the Kunlunshan earthquake (M_s 8.1), northern Tibetan Plateau, China, *Seismol. Res. Lett.*, *73*, 884–892.

Yeats, R. S., K. Sieh, and C. R. Allen (1997), *The Geology of Earthquakes*, 568 pp., Oxford Univ. Press, New York.

C. Brough, S. Das, and D. P. Robinson, Department of Earth Sciences, University of Oxford, Parks Road, Oxford OX1 3PR, UK. (christopher.brough@gmail.com; das@earth.ox.ac.uk; davidr@earth.ox.ac.uk)